Observation of Kondo-like electrical transport in ferromagnetic $Fe_2Ti_{1-x}Mn_xSn$ Heusler alloy

Kulbhushan Mishra [1], Shishir Kumar Pandey [2], S. Chaudhuri [3,*], Rajeev Rawat [4] and P. A. Bhobe [1,†]

[1] *Indian Institute of Technology Indore, Khandwa Road, Simrol, Indore 453552, India*

[2] *Department of General Sciences (Physics), Birla Institute of Technology and Science, Pilani, Dubai Campus, Dubai International Academic City, Dubai 345055, United Arab Emirates*

[3] *Center for Condensed Matter Science, National Taiwan University, Taipei 10617, Taiwan*

[4] *UGC-DAE Consortium for Scientific Research, University Campus, Khandwa Road, Indore 452001, India*

(Received 25 February 2025; revised 6 June 2025; accepted 10 June 2025; published 27 June 2025)

We investigate the effect of Mn substitution on the electronic, magnetic, and electrical transport properties of $Fe_2Ti_{1-x}Mn_xSn$. Spin-polarized density of states calculations using density functional theory indicate a half-metallic ground state in Mn-rich compositions. Localized magnetic moments at Mn sites interact through the conduction electron cloud. Electrical resistivity and magnetotransport measurements show dominant Kondo-like scattering at low temperatures alongside a distinctive linear negative temperature coefficient of resistance at higher temperatures. These findings are further supported by specific heat measurements. Isothermal magnetization as a function of the applied magnetic field identifies the magnetic ground state of $Fe_2Ti_{1-x}Mn_xSn$ compositions as a ferromagnet with a wandering axis that aligns with the direction of the applied field. Temperature-dependent magnetization measurements highlight features indicative of weak anisotropy in the system, while the x-ray diffraction analysis reveals a highly ordered cubic structure with reduced antisite disorder. Investigation of the local crystal structure using x-ray absorption fine structure spectroscopy shows that the random anisotropy arises from local lattice distortions around Mn atoms. These findings shed light on the emergence of a spin-polarized band structure and a unique magnetic ground state in Mn-substituted $Fe_2Ti_{1-x}Mn_xSn$, offering insights into spintronic materials.

DOI: 10.1103/jnxr-9qf8

I. INTRODUCTION

It has long been recognized that localized magnetic moments in metals interact through Ruderman-Kittel-Kasuya-Yosida (RKKY) interactions, mediated by the conduction electrons [1–3]. However, when a local moment is coupled to the sea of conduction electrons, the Kondo effect can emerge at low enough temperatures, significantly altering the electronic structure and, therefore, dramatically impacting the transport properties of the system. In heavy-fermion compounds, the coupling between local moment and conduction electrons typically gives rise to two competing mechanisms: the intrasite Kondo screening and intersite long-range RKKY interactions. The RKKY interaction favors a magnetically ordered state, while the Kondo screening is considered to form a nonmagnetic heavy fermion state. Thus, a simultaneous occurrence of the Kondo effect and ferromagnetism in certain materials presents a fascinating and complex problem in condensed matter physics. Recently, weak ferromagnetism below the Kondo temperature has been observed near the magnetic phase transition in Kondo lattice materials [4–6]. The simultaneous occurrence of these two mutually exclusive phenomena is highly intriguing from a fundamental perspective and highly relevant for potential applications [7]. Interestingly, the simultaneous observation of the Kondo effect and ferromagnetism in transition metal compounds is exceptionally rare.

Transition metal-based Heusler alloys have been intensively studied due to their unique physical properties, which include magnetic shape memory effect [8], near-room temperature magnetocaloric effect [9], half-metallic ferromagnetism [10,11], spin-gapless semiconductivity, unconventional superconductivity [12], thermoelectricity [13,14], and anomalous Hall effect, heavy fermion, non-Fermi liquid properties, and the Kondo effect, among others. Heusler alloys (general formula: X_2YZ) crystallize in the $L2_1$ structure (space group $Fm\bar{3}m$) consisting of four interpenetrating FCC sublattices, where the X atom occupies the (0.25,0.25,0.25) and (0.75,0.75,0.75) sublattice sites, whereas the Y and Z atoms occupy the (0.5,0.5,0.5) and (0,0,0) sublattice sites, respectively. Theoretical studies on Heusler alloys reveal an interesting relationship between the total spin moment per unit cell (M_T) and the number of valence electrons count (VEC) per formula unit (Z). Also known as the Slater-Pauling rule [15], this relationship states the quantitative value of M_T as equal to (Z-24) and seems to provide a handle to modulate the physical properties of Heuslers through suitable chemical substitutions.

A notable example of the Heusler family is the Fe_2TiSn composition, which conforms to VEC = 24. The electronic structure calculation indicates Fe_2TiSn to be a nonmagnetic semimetal with a pseudogap in the density of states (DOS)

*Present address: GITAM University, Rudraram, Hyderabad, Telangana 502329, India.

†Contact author: pbhobe@iiti.ac.in

 ©2025 American Physical Society

TABLE I. Atomic percentages, parameters determining goodness of fit, and magnetic transition temperatures of $Fe_2Ti_{1-x}Mn_xSn$.

Composition	Atomic %				Goodness of fit			T_C	T_S
	Fe	Ti	Mn	Sn	R_{Bragg}	R_F	χ^2	(K)	(K)
0.05	48.05	24.51	1.23	26.21	8.12	10.1	1.94	<5	250
0.10	48.29	22.76	2.55	26.27	8.44	6.49	2.51	6	268
0.25	48.0	19.55	6.25	26.13	9.68	7.86	2.77	18	320
0.30	47.91	18.10	7.40	26.60	10.7	9.09	2.02	25	325

at the Fermi level. However, a change in the DOS at the Fermi level due to the local environment of Fe, because of antisite disorder between Fe and Ti sites, leads to the superparamagnetic ground state at low temperature [16]. Based on specific heat measurements, it has been speculated to be a heavy fermion metal with quasiparticle mass $\sim 40\ m_e$ [17]. A comparison of the x-ray photoelectron spectroscopy valence-band spectra with band-structure calculations, both with and without atomic disorder, indicates that the weak ferromagnetism and heavy-fermion behavior in Fe_2TiSn are driven by the presence of atomic disorder [17]. Further, the substitution of Ni at the Fe site forms a system with isolated spins, leading to a Kondo-like interaction between localized spins and conduction electrons. On the contrary, Co substitution leads to a typical spin fluctuation scenario [18]. It is to be noted here that in contrast to Fe and Co, bulk Ni has a sharp peak at E_F in one of the spin subbands [19]. This sudden increase of DOS at E_F may lead to enhanced electron correlation, leading to Kondo-like spin scattering at low temperatures. It has also been found that with proper substitution at Ti and Sn sites, the system can be driven to half-metallicity [20,21]. These observations suggest that the nonmagnetic semimetallic band structure of Fe_2TiSn is highly sensitive to doping or elemental substitution, and an interesting ground state may emerge upon suitable substitution.

In this paper, we report a detailed investigation of the structural, magnetic, and transport properties of Mn-substituted Fe_2TiSn compositions. X-ray diffraction (XRD) results show the formation of an ordered $L2_1$ structure with reduced antisite disorder. The low-temperature upturn in the electrical resistivity is due to the Kondo-like spin scattering. This interpretation is further supported by specific heat measurements. The temperature- and field-dependent magnetization measurements indicate the presence of anisotropy in the system due to the strong local magnetic moment of Mn atoms. Additionally, EXAFS measurements indicate that the magnetocrystalline anisotropy in the cubic Heusler compound primarily originates from local lattice distortions. We have also performed electronic structure calculations to better understand the ground state properties.

II. EXPERIMENTAL AND COMPUTATIONAL DETAILS

Polycrystalline $Fe_2Ti_{1-x}Mn_xSn$ compositions were prepared by melting stoichiometric amounts of high-purity (99.99%) elements such as Fe, Mn, Ti, and Sn using an electric arc furnace by placing these elements on a water-cooled Cu hearth and under a flowing Ar atmosphere. The homogeneous ingots thus formed were vacuum sealed in the quartz tubes and annealed for 72 hours at 800 °C followed by quenching in ice water. The weight loss of all the prepared compositions is consistent and well below 1%. The energy dispersive x-ray spectroscopy, equipped with a field emission scanning electron microscope, was performed using Model FE-SEM Supra 55 (Carl Zeiss, Germany) to ensure the target composition after melting was close to the starting stoichiometry. The atomic percentages of the elements are presented in Table I, and the elemental mapping for $x = 0.25$ is shown in Fig. 1. The crystallographic phase purity of the samples was checked using a laboratory x-ray source on a Bruker D8 Advance diffractometer having a Cu target ($\lambda = 1.5406$ Å), confirming the formation of the Heusler phase. Magnetization as a function of temperature and magnetic field was measured using a Quantum Design SQUID magnetometer. A standard four-probe method with a homemade resistivity setup equipped with a superconducting magnet system was used for the electrical resistivity and magnetoresistance measurements. The extended x-ray absorption fine structure (EXAFS) measurement was carried out at P65 beamline, PETRA-III DESY, Hamburg, Germany at Fe (7112 eV) and Ti (4966 eV) K edges at 6 K. Gas-filled ionization chambers were used to simultaneously record the incident (I_0) and transmitted (I) photon energies. The data was collected over various scans to reduce the statistical noise. Subsequently, the EXAFS signal was extracted and analyzed in the 3 to 14 $Å^{-1}$ range using the DEMETER suite [22].

Density-functional theory (DFT) calculations were performed within the QUANTUM ESPRESSO package [23,24] where ultrasoft pseudopotentials [25] and a plane-wave basis set are employed. Generalized-gradient approximation with

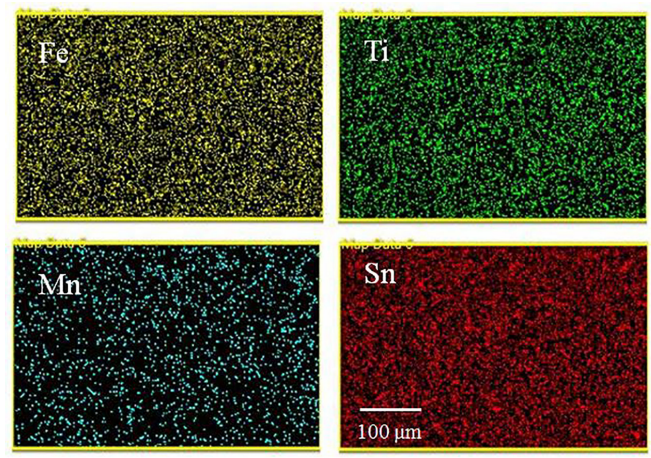


FIG. 1. The elemental mapping results of $x = 0.25$. The figures are presented at a scale of 100 µm.

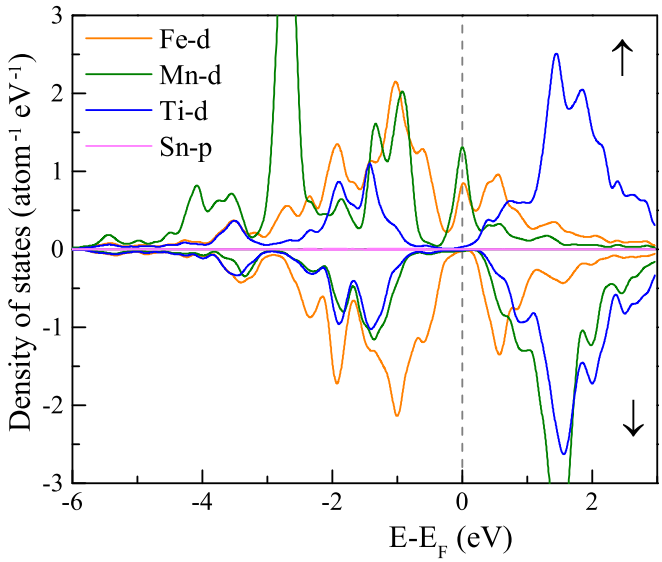


FIG. 2. Atom-projected spin-polarized density of states for Fe, Mn, and Ti -*d* and Sn *p* orbitals in $Fe_2Ti_{0.75}Mn_{0.25}Sn$ in the ferromagnetic arrangements. Contributions from Fe and Mn *d* states in the up-spin channel at the Fermi level (set to zero) signify the itinerant magnetic interaction between these two atoms. Contributions from Ti *d* and Sn *p* orbitals are either below or above the Fermi level.

Perdew–Burke–Ernzerhof functional form is used for the calculation of exchange-correlation energy [26]. The kinetic energy cutoff for plane-wave functions of 95 Ry and the charge density of 1140 Ry are considered in our calculations. We start with the simple cubic crystal structure (space group $Fm-3m$, No. 225) of Fe_2TiSn with lattice constant $a = 6.059$ Å and fully optimize it after replacing one of the Ti atoms with Mn (25% doping). Energy convergence criterion of 5×10^{-7} Ry and 6×6×6 uniform *k* mesh and Marzari-Vanderbilt smearing are considered in our calculations. The optimization leads to small changes (<1.0%) in the lattice constants. These spin-polarized calculations start by aligning all eight Fe atoms ferromagnetically with large moments while one Mn atom is aligned antiferromagnetically with the Fe atoms in the 16-atom unit cell. However, after the convergence, the negligibly small Fe and large Mn magnetic moments are aligned ferromagnetically. We discuss these results in connection with the magnetic properties of the compositions at a later stage.

For the present calculation, the Mn-Mn magnetic interaction is estimated by considering 2×2×2 supercell of 128 atoms and replacing two Ti atoms with Mn. The different separation between these two Mn atoms within this supercell is then considered to extract the distance-dependent magnetic interaction. The four possible Mn-Mn separations considered, after avoiding the possible interference of periodic images of supercell on magnetic interactions, are 4.254 Å, 6.017 Å, 7.369 Å, and 8.509 Å. At these four distances, magnetic interaction is estimated by calculating the energy difference between ferromagnetic and antiferromagnetic arrangements of the two Mn atoms. Background from negligibly small Fe and Ti magnetic moments has an insignificant influence on the magnetic interactions estimated in this fashion.

III. RESULTS AND DISCUSSION

The DOS scenario of the $Fe_2Ti_{1-x}Mn_xSn$ system is obtained using a DFT-only approach. For this case, the atom-projected spin-polarized DOS of Fe, Mn, Ti -*d*, and Sn *p* states are shown in Fig. 2. Many insightful observations can be made from this plot. First, the system shows the half-metallic character of the DOS with mainly Fe and Mn *d* states in the spin-up channel, while there is a band gap in the spin-down channel at the Fermi level. Though Ti *d* states also contribute below the Fermi level, the dominant contributors remain the *d* states of Fe and Mn atoms, and the magnetic properties arise from the interactions among all three transition metal atoms. Second, this interaction can be considered itinerant as the system is metallic. Third, the magnetic moment on the Mn site is large, while Fe and Ti atoms carry negligible moments, and both Mn and Fe have finite contributions to the DOS at the Fermi level. Recall that we started with a scenario of antiferromagnetic coupling between single Mn and eight (ferromagnetically aligned) Fe atoms. Such a system converges to a ferromagnetic coupling among all the magnetic atoms, with negligibly small magnetic moments on Fe ($\sim 0.016\ \mu_B$) and Ti ($\sim 0.052\ \mu_B$) atoms and a relatively high moment on Mn

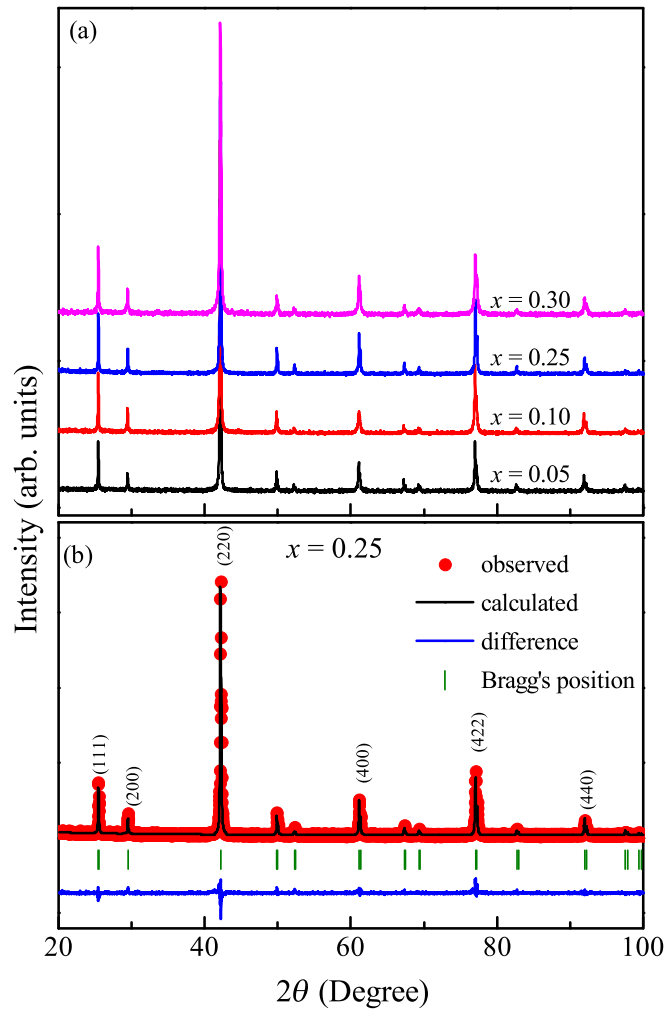


FIG. 3. (a) X-ray diffraction profile of $Fe_2Ti_{1-x}Mn_xSn$, and (b) Rietveld refined XRD profile of $x = 0.25$.

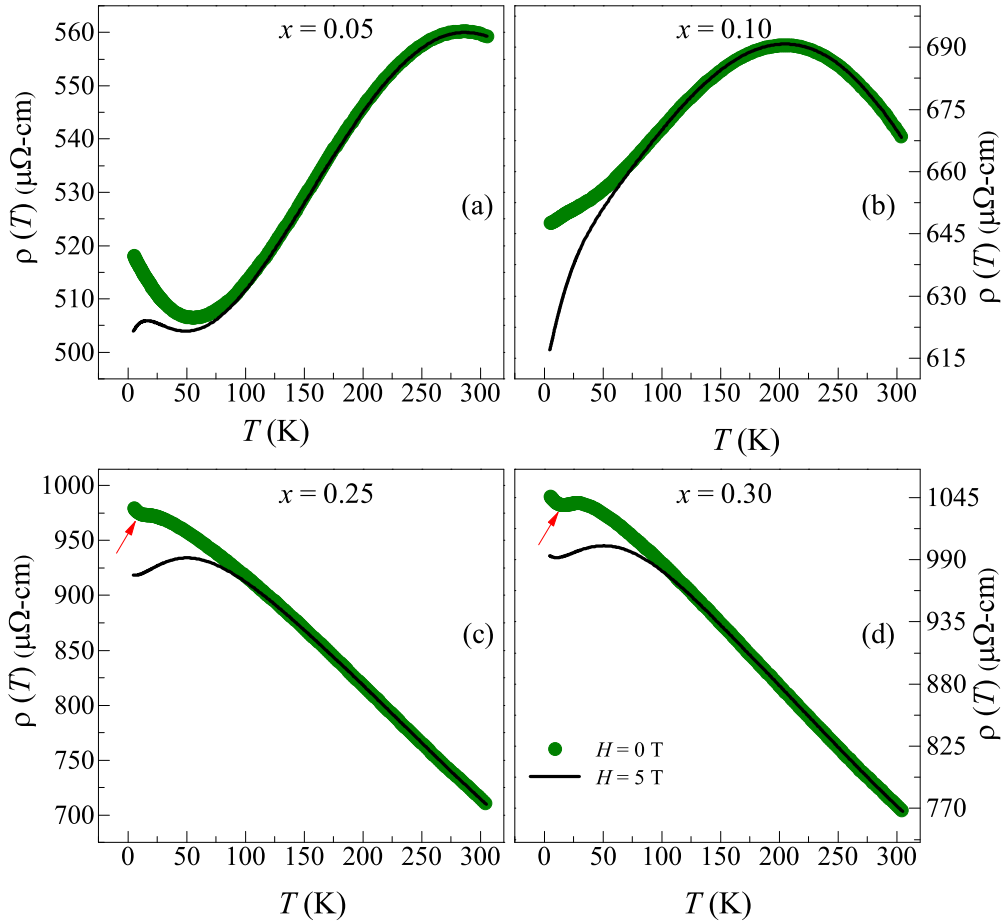


FIG. 4. Temperature-dependent electrical resistivity of $Fe_2Ti_{1-x}Mn_xSn$ measured at an applied magnetic field of 0 T and 5 T.

($\sim 3.161\ \mu_B$) atoms. It appears as if Mn atoms are the ones with localized moments that are interacting through the cloud of conduction electrons formed by Fe and Ti atoms.

Further, to explore the effect of Mn substitution on structural, transport, and magnetic properties of Fe_2TiSn, we begin the experimental investigation into the Mn–substituted Fe_2TiSn compounds. The XRD patterns of $Fe_2Ti_{1-x}Mn_xSn$ ($x = 0.05$, 0.1, 0.25, and 0.3) are shown in Fig. 3(a). The presence of strong (111), (200), and (220) peaks confirm the highly ordered cubic $L2_1$ crystal structure in all the prepared compositions. However, the solubility limit of Mn in Fe_2TiSn is limited to 30% as additional peaks related to the secondary phase begin to appear for compositions with $x \geqslant 0.4$. Contrary to the general expectation of finding an increase in the antisite disorder upon carrying out substitutions in an intermetallic system, the present compositions show a relative increase in the intensity of the (111) and (200) superlattice peaks, indicating a reduction of the overall disorder in comparison to pristine Fe_2TiSn. Rietveld refinement of the XRD profiles, implemented through the FULLPROF suite [27], yield values for lattice parameters that follow Vegard's law [28], indicating the desired substitutions at the targeted lattice sites have indeed been achieved.

With the prediction of half-metallic DOS at the Fermi level and a highly ordered crystal structure, studying the electrical resistivity of the Mn-substituted Fe_2TiSn compounds becomes pertinent. It has been previously observed that the electrical resistivity, $\rho(T)$, of Fe_2TiSn shows a bad metallic behavior with a low-temperature upturn and a minimum at 50 K. This low-temperature upturn in $\rho(T)$ is due to weak localization (WL) caused by antisite disorder between the Fe and Ti sites. Figure 4 shows the $\rho(T)$ data for $Fe_2Ti_{1-x}Mn_xSn$ ($x = 0.05$, 0.10, 0.25, 0.30) for a temperature range of 5–300 K and measured under applied magnetic fields of 0 T and 5 T. Although the overall features of the $\rho(T)$ curve for the $x = 0.05$ sample are a close match to those observed for Fe_2TiSn, the addition of Mn results in the rise of the overall resistivity. This behavior can be understood by considering the inherently p-type nature of Fe_2TiSn, where charge transport is inherently governed by holes [16]. When Mn substitutes for Ti, it introduces additional electrons into the system, which partially compensate the existing hole carriers. This compensation reduces the net carrier density, thereby increasing the electrical resistivity upon Mn substitution (see Fig. S3(a) in the Supplemental Material [29]). Notably, this increase in resistivity deviates from the conventional metallic behavior typically expected with electron doping. Furthermore, the $\rho(T)$ curve for the $x = 0.10$ composition exhibits a negative temperature coefficient of resistance (TCR) down to approximately 200 K, transitioning to a positive TCR at lower temperatures. On the other hand, $x = 0.25$ and 0.30 compositions exhibit complete negative TCR throughout the measurement range. A closer inspection reveals that the $\rho(T)$ of $x = 0.25$ and 0.30 shows a weak slope change at low

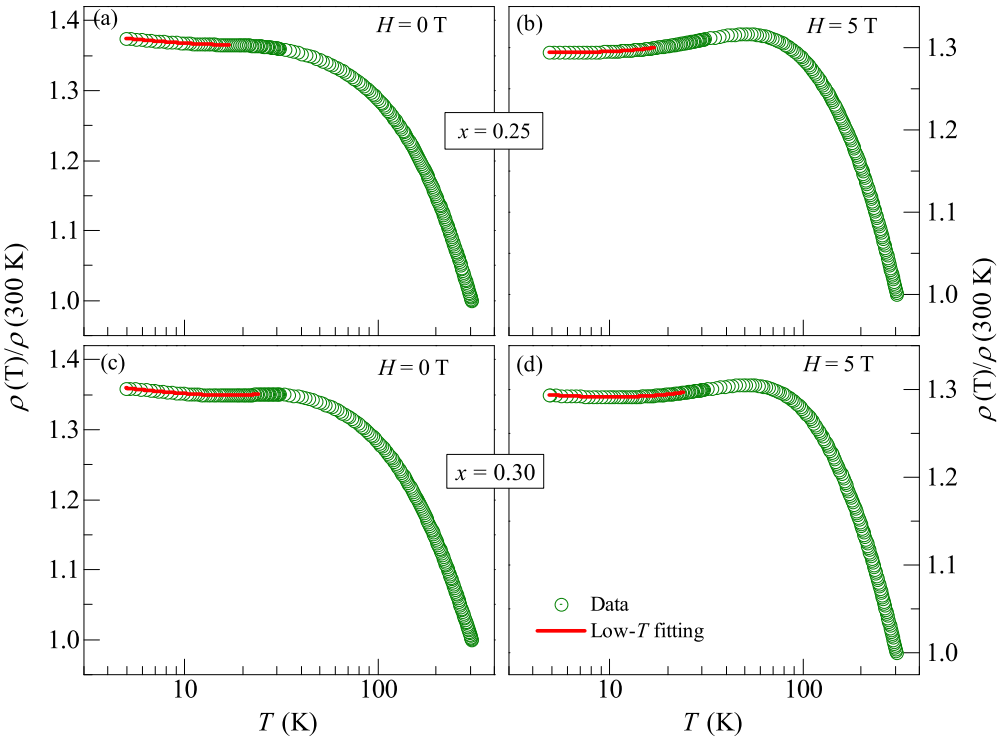


FIG. 5. (a)–(d) Fitting of temperature-dependent resistivity data of $x = 0.25$ and 0.30 at 0 T and 5 T, respectively. The temperature axis is represented on a log scale for better visibility of the low-T fitting.

temperature (indicated by arrow), below which $\rho(T)$ increases at a faster rate with decreasing temperature.

The low-temperature data are analyzed by considering the different scattering mechanisms that may contribute to the observed $\rho(T)$ behavior. A low-T upturn in resistivity can result from various mechanisms, including electron-electron interaction (EEI), weak localization (WL), and Kondo-like transport. EEI arises from electron-electron elastic scattering due to the Coulomb interaction between conduction electrons, WL arises from disorder-mediated coherent backscattering of charge carriers, and Kondo-like transport arises from the interaction between the localized magnetic moment associated with the magnetic impurities and mobile conduction electrons [4,30]. In Mn-substituted Fe_2TiSn, a reduction in atomic disorder and/or magnetic order destroys the WL, suggesting that the low-T upturn of $\rho(T)$ in compositions with higher Mn concentration is not caused by WL [16,31]. Furthermore, we separately fit the $\rho(T)$ data with EEI and Kondo effect (see Fig. S3(c) in Supplemental Material [29]). As the result indicates, neither model fits the experimental data satisfactorily. Thus, combining both mechanisms likely contributes to the observed low-T upturn in resistivity. Besides, the contribution from electron-phonon scattering should also be added to the form T^5 to represent the resistivity [32]. Thus, the low-T resistivity data at $H = 0$ T and 5 T can be described by the expression $\rho(T) = \rho_0 + \rho_e T^{1/2} - \rho_K \ln(T) + \rho_p T^5$, where, ρ_0 is residual resistivity, and, ρ_e, ρ_K and ρ_p represent coefficients for EEI, Kondo-like transport, and electron-phonon scattering, respectively. The fitting result is shown in Fig. 5, and the fitting parameters for different Mn substitution and applied magnetic field are depicted in Table II. To make a better comparison across different compositions, the fitting was performed on the normalized resistivity data (see Fig. S3(b) in the Supplemental Material [29]). It is evident from the Table II that both ρ_e and ρ_K increase with increasing x. Further, the value of ρ_K (i) is higher than ρ_e and (ii) is higher at $H = 0$ T compared to 5 T for a given composition. This highlights the dominant role of Kondo-like scattering of charge carriers in $Fe_2Ti_{1-x}Mn_xSn$ for $x \geqslant 0.25$ compared to EEI.

Next, we analyze the $\rho(T)$ behavior of $x = 0.25$(and 0.30) composition in the high-T region. While the negative TCR has been observed in Heusler compounds [33–37], the notable feature here is the linear $\rho(T)$ between 100 K and 300 K, which is unusual compared to the common semiconductor and disordered metallic systems. In semiconductors, electron transport exhibits a thermally activated behavior of $\rho(T)$ data where the ρ vs T plot is upward convex. On the contrary, disordered metallic systems show a convex downward behavior of $\rho(T)$ data. Further, reports on the high-T resistivity data of Fe_2TiSn show a negative TCR from 300 K to 800 K, which is attributed to the interband transition of conduction electrons through a gap at the Fermi level [38]. With electron doping in pristine Fe_2TiSn, this negative TCR persists below 300 K [18] and may also result in half-metallicity [20,21]. A similar

TABLE II. The extracted parameters after fitting the ρ(T) data in low-temperature regions for the applied fields of 0 and 5 T.

x	ρ_0		$\rho_e \times 10^{-2}$		$\rho_K \times 10^{-2}$		$\rho_p \times 10^{-9}$	
	0 T	5 T	0 T	5 T	0 T	5 T	0 T	5 T
0.25	1.389	1.292	0.67	1.20	1.89	1.7	1.239	0.73
0.30	1.376	1.297	1.01	1.24	2.5	1.9	0.397	0.135

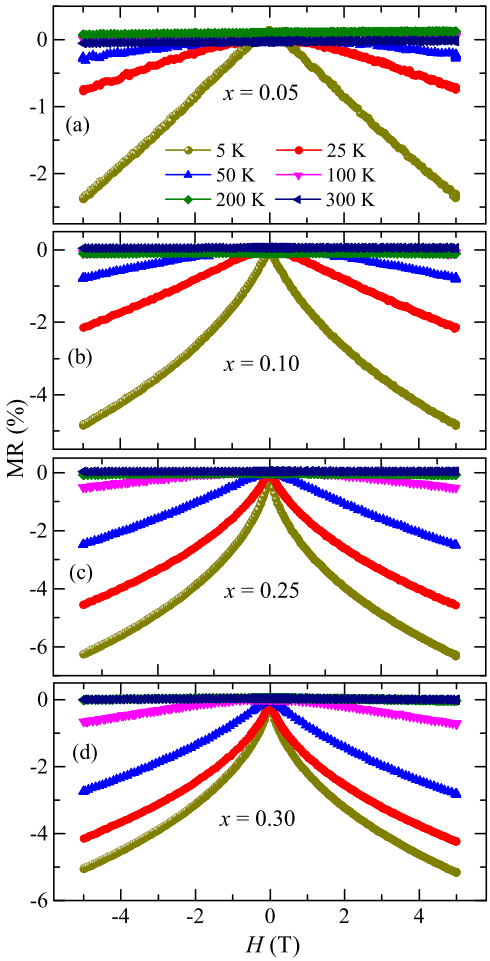


FIG. 6. Field-dependent isothermal magnetoresistance, MR, of $Fe_2Ti_{1-x}Mn_xSn$.

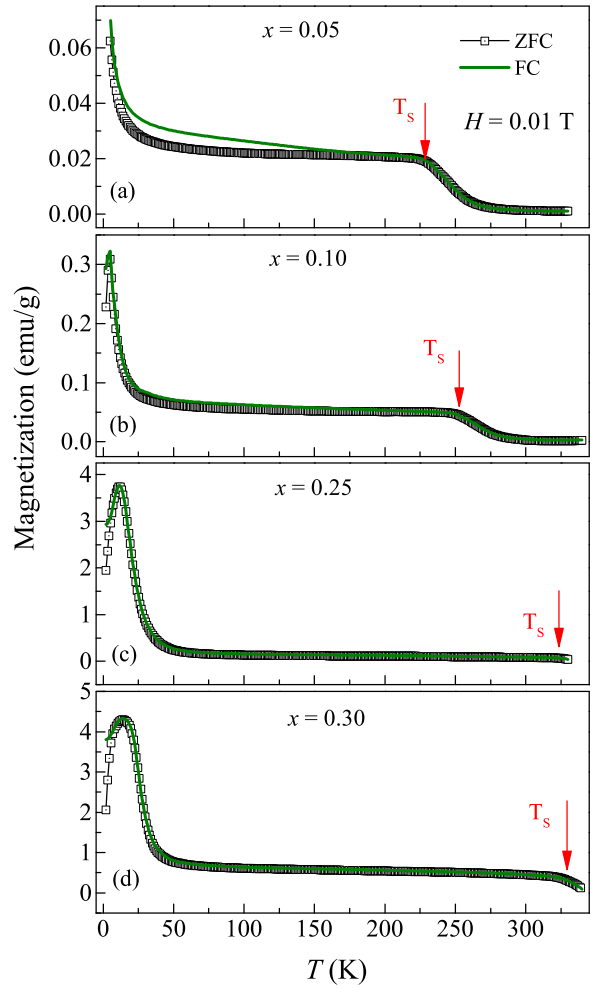


FIG. 7. Temperature dependence of the magnetization, $M(T)$ curves, of (a) $x = 0.05$, (b) $x = 0.10$, (c) $x = 0.25$, and (d) $x = 0.30$.

signature is observed in the present $Fe_2Ti_{1-x}Mn_xSn$ compositions. Thus, the combined results of theoretical calculations and electrical resistivity strongly suggest the presence of half metallicity in Mn-substituted Fe_2TiSn.

Figure 6 shows the isothermal magnetoresistance (MR) curves measured at different temperatures ranging from 5 K $\leqslant T \leqslant$ 300 K and for all four compositions. Using the standard definition of MR as $\mathrm{MR}(\%) = [\frac{\rho(H)-\rho(0)}{\rho(0)}]\times 100$, we find that all the Mn–substituted compositions show the isotropic negative MR in the entire temperature range. Generally, the field-dependent resistivity, $\rho(T, H)$, depends on the combined sum of Lorentz force and the contribution from different scattering mechanisms. The Lorentz force constitutes the classical MR, which is inherently positive. However, the observed small yet negative MR at high temperatures is attributed to the presence of short-range ferromagnetic correlations, as will be discussed later.

Moreover, the increase in the magnitude of MR at low temperatures with increasing Mn content suggests the presence of magnetic ordering and/or spin-dependent scattering. Additionally, compositions showing signatures of half-metallicity, i.e., $x = 0.25$ (and 0.30), exhibit the dominance of the Kondo-like scattering in low-T resistivity. Notably, the EEI effect leads to a positive MR due to Zeeman splitting and orbital effects, with its magnitude varying as the square root of the applied magnetic field [30,39–42]. This has been reflected as the increment of the ρ_e value with an applied magnetic field of 5 T for a given value of x (see Table II). Conversely, applying the magnetic field suppresses the fluctuation in the localized magnetic moment and spin-dependent scattering, leading to a negative MR in a Kondo system [43]. Thus, for $x = 0.25$ (and 0.30), the negative MR supports that the Kondo effect is the dominant mechanism governing the low-T electrical resistivity. This also explains the higher value of ρ_k compared to the ρ_e obtained from fitting the low-T resistivity data.

Having understood the electronic DOS in the $Fe_2Ti_{1-x}Mn_xSn$ compositions and possible half-metallic ground state in $x \geqslant 0.25$, we now discuss the experimental study of its magnetic properties. The temperature-dependent magnetization, $M(T)$, measured at $H = 0.01$ T, is plotted in Fig. 7. According to previous studies, an inherent Fe-Ti antisite disorder in the otherwise nonmagnetic Fe_2TiSn induces the formation of weak magnetic clusters [16]. These interactions are identified by a steplike feature in the high-temperature region, denoted here as T_S, in the $M(T)$ curve. This steplike feature shifts toward the high-temperature side with rising Mn substitution. Additionally, an abrupt rise

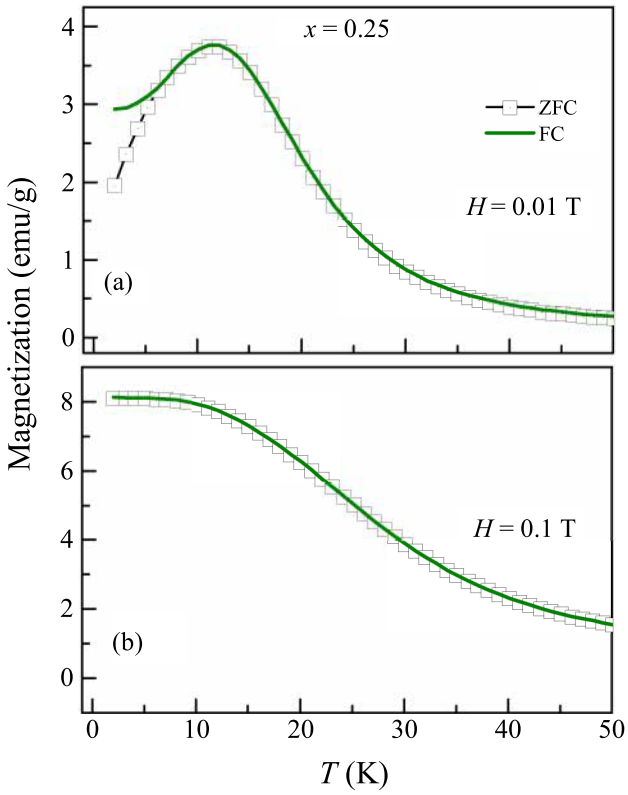


FIG. 8. Temperature dependence of the magnetization, $M(T)$ curves, of $x = 0.25$ at an applied magnetic field of (a) $H = 0.01$ T, and (b) $H = 0.1$ T.

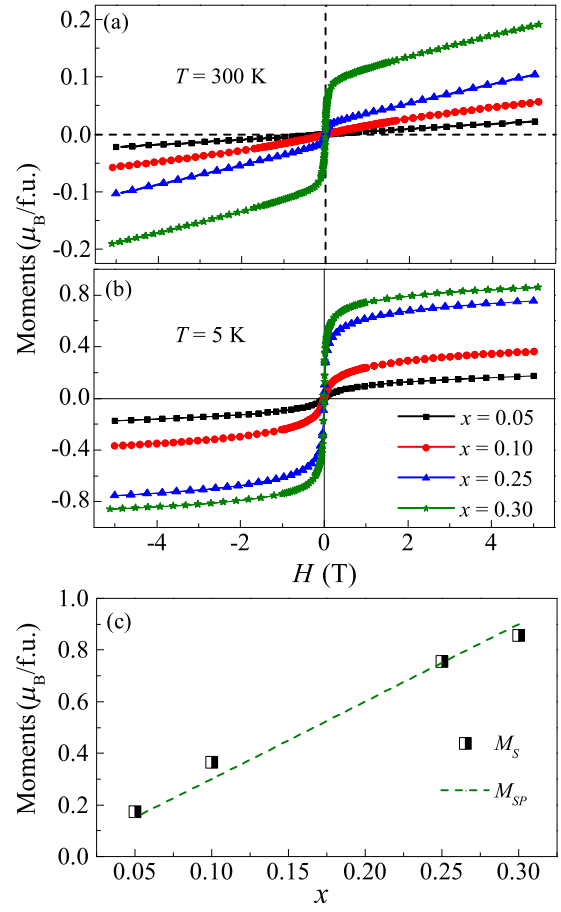


FIG. 9. Isothermal magnetization, $M(H)$ curve of all the compositions measured at (a) 300 K, (b) 5 K. (c) Values of experimental magnetic moment per formula unit at the maximum applied field (M_S) at $T = 5$ K, for different Mn concentrations. The dashed line shows the moment values as predicted by Slater-Pauling rule.

in magnetization is observed at low temperatures, marking the transition to a magnetically ordered state. This temperature is identified as T_C, and its value increases with rising Mn content. The values of T_C and T_S are listed in Table I.

Figure 8 shows the magnified view of the $M(T)$ curve for $x = 0.25$, measured at two different applied magnetic fields. At a low applied magnetic field (0.01 T), there is a noticeable contrast between the $M(T)$ plots recorded during the zero field-cooled (ZFC) and field-cooled (FC) protocols. This bifurcation between ZFC/FC disappears when a relatively strong magnetic field of $\geqslant 0.1$ T is applied, suggesting the presence of weak anisotropy in the material. In the ZFC process, the material's anisotropy determines the amount of magnetization below T_C and may prevent a relatively small applied field from aligning the moments in the direction of the field. When the same material is cooled through T_C while being exposed to a magnetic field during the FC process, the moments are locked into the direction of the applied magnetic field. As a result, there is a noticeable contrast between the ZFC and FC curves for small applied fields, and this bifurcation disappears when a slightly stronger magnetic field is applied.

Figures 9(a) and 9(b) show the variation of isothermal magnetization (M) as a function of the applied magnetic field (H) for all the compositions measured at 300 K and 5 K, respectively. For $x = 0.05$, the $M(H)$ curve at 300 K displays a linear behavior [Fig. 9(a)]. With increasing x, a sharp rise in M is observed at lower fields, followed by a linear behavior at higher fields, suggesting the presence of short-range ferromagnetic correlations at room temperature. Further, at $T = 5$ K, the $M(H)$ curve shows the characteristics of a ferromagnetic ordering with an increase in the magnetic moment values with x [see Fig. 9(b)]. The value of the experimental magnetic moment per formula unit (M_S) at $H = 5$ T aligns well with the theoretical value predicted by the Slater-Pauling rule [Fig. 9(c)]. While the $M(H)$ curves do not show complete saturation, this agreement provides strong evidence for a spin-polarized band structure in $Fe_2Ti_{1-x}Mn_xSn$.

Additionally, the presence of ferromagnetic clusters at $T = 300$ K suggests that the low-temperature magnetization behavior could be solely due to the evolution of these clusters. To interpret this, we have fitted the $M(H)$ curve at 5 K using the modified Langevin function, expressed as $M(H) = M_sL(\alpha) + \chi H$, where $\alpha = \mu \mathrm{H}/\mathrm{k}_B\mathrm{T}$, M_S represents the saturation magnetization, μ is the average magnetic moment and χ represents the paramagnetic susceptibility. The lack of fit of this model to the data (see Fig. S4 in the Supplemental Material [29]) rules out any clusterlike evolution in the prepared compositions. Alternatively, it appears that the Mn-substituted Fe_2TiSn compositions display a long-range ferromagnetic order below T_C, which exhibits a substantial

dependency on the strength of the applied magnetic field with respect to the random anisotropy. Interestingly, in contrast to this behavior, Mn-substituted Fe_2VAl exhibits antiferromagnetic ordering [44], primarily due to the difference in the structural order, comprising sizable $B2$ disorder and a shorter Mn-Mn separation [45].

Taken together, these findings highlight the subtle interplay between structural order and magnetic interactions in Fe-Mn-based Heusler systems. In particular, the field-dependent magnetic behavior observed in Mn-substituted Fe_2TiSn suggests that the weak random anisotropy model [46] could be applicable in describing the low-temperature magnetic properties of these compositions. Such a model has previously been extensively used to explain the FM correlations in Heusler alloys [47–49]. This model incorporates both the experimentally applied magnetic field and the ground state configuration of magnetic materials with random anisotropy for a wide range of anisotropy strengths. Three distinct regimes can be identified for the weak anisotropy situation based on the magnitude of the applied magnetic field, H, and the parameter H_S $(= H_r^4/H_{\text{ex}}^3)$, where H_r and H_{ex} are anisotropic and exchange fields, respectively. For $H < H_S$, one obtains a correlated spin glass phase with a high magnetic susceptibility for low fields. When $H_S < H < H_{\text{ex}}$, a ferromagnet with a wandering axis (FMWA) results from a rough alignment of the spins in the presence of a weak magnetic field. The tipping angle of the magnetization vector, with respect to the applied magnetic field, changes throughout the system due to the noncollinear magnetic structure. In this regime, the magnetization approaches saturation as

$$M(H) = M_s\left[1 - \frac{1}{15}\left(\frac{H_s}{H + H_c}\right)^{\frac{1}{2}}\right], \tag{1}$$

where M_s is saturation magnetization, and H_c is the field due to the coherent portion of the anisotropy. In the third regime, where $H \gg H_S$, the correlation length of the spins reduces as the field strength increases, whereas the tipping angle is completely uncorrelated among sites. Except for a slight tipping angle (less than in the case of FMWA) brought on by random anisotropy, all spins in this regime are almost aligned with the field. In such cases, isothermal magnetization gradually approaches saturation as

$$M(H) = M_s\left[1 - \frac{1}{15}\left(\frac{H_r}{H + H_{\text{ex}}}\right)^{2}\right]. \tag{2}$$

We have fitted our data using Eq. (1) with an additional paramagnetic contribution, χH [50], to the $M(H)$ curve at 5 K of $x = 0.25$, as shown by the solid line in Fig. 10. It shows a satisfactory fit for a wide range of applied fields from 0.4 to 5 T. The value of H_s derived after the fitting ranges from 0.303 T for $x = 0.05$ to 0.021 T for $x = 0.30$, which is lower than the maximum applied field, following the condition for the system to fall in the second regime. In contrast, Eq. (2) does not yield a good fit to the data [see the dashed line in Fig. 10(a)], and the value of H_s derived after the fitting is much higher than the maximum applied field despite using the prefactor equal to 1 instead of 1/15 [48]. Thus, the magnetic properties confirm that the low-T magnetic ground

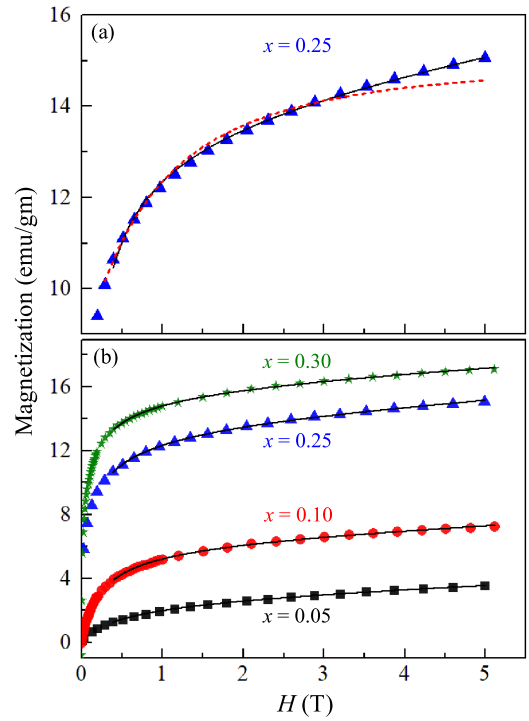


FIG. 10. Fitting of $M(H)$ curve at $T = 5$ K with random anisotropy model for (a) $x = 0.25$ and (b) for all compositions. The solid line shows the fitting with Eq. (1), and the dashed line shows the fitting to Eq. (2). See the text for more details.

state can be well described by the random anisotropy model, with a ferromagneticlike ordering present below T_C, particularly for $x \geqslant 0.25$. Although the $M(H)$ curve at $T = 5$ K does not saturate even under an applied magnetic field of 5 T, the experimental magnetization (M_S) reaches its maximum theoretical value (M_{SP}) predicted by the Slater-Pauling rule. Achieving M_{SP} would require complete ferromagnetic ordering, which is inconsistent with the wandering axis ferromagnet scenario. Additionally, while the primary contribution arises from the intrinsic magnetic structure, the possible influence of high-temperature superparamagnetic clusters on the low-temperature $M(H)$ curve cannot be entirely ruled out.

Random anisotropy in cubic systems can occur from substitutional impurities and disorder [51]. In Ref. [50], Gehring *et al.* proposed that the random anisotropy in cubic polycrystalline $Dy_{1-x}Y_xAl_2$ could originate from lowering of local lattice symmetry, driven by lattice mismatch, difference in charge screening, and spin-orbit interactions [50]. In certain cubic Heusler systems, such random anisotropy is found to influence their low-temperature magnetic properties [47]. To unravel the reason that the random anisotropy in our cubic $Fe_2Ti_{1-x}Mn_xSn$ originates from local lattice distortion, we undertake measurement of the high-resolution synchrotron-based EXAFS spectra at Fe and Ti K-edges for $x = 0.25$. The EXAFS data is extracted in the reciprocal space, $\chi(k)$, and Fourier transformed to real space, $\chi(R)$, where the magnitude and real part of $\chi(R)$ reflect the radial distribution function around the absorbing atoms. The local structural refinement is carried out by varying the atomic distances and thermal mean square factor (σ^2) until a good fit is obtained in the

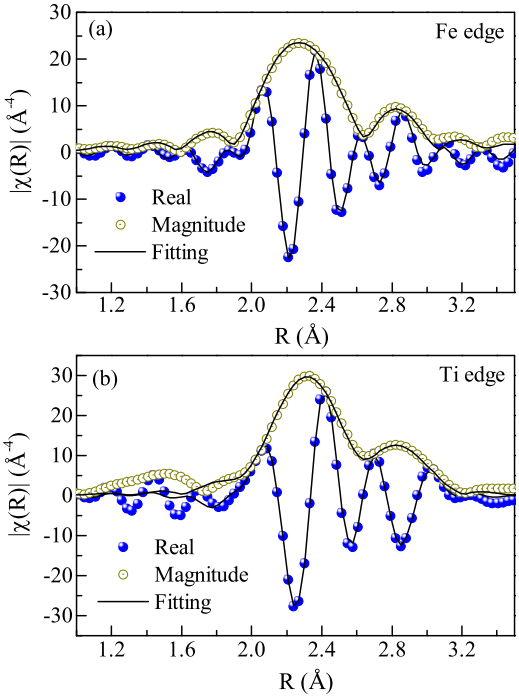


FIG. 11. Magnitude (hollow spheres) and real component (solid spheres) of Fourier-transformed (a) Fe and (b) Ti K edge EXAFS spectra at 6 K for $x = 0.25$. See the text for details.

range of 1.8–3.0 Å in the R space and 3 to 14 Å^{-1} in k space. Based on the information extracted from the XRD profile of the cubic $L2_1$ structure and lattice constant of 6.059 Å, the local atomic arrangement around the Fe atom has four Ti and four Sn atoms at an equal distance of ∼2.623 Å, and six Fe atoms at ∼3.029 Å. Similarly, for the Ti atom, there are eight Fe atoms at ∼2.623 Å and six Sn atoms at ∼ 3.029 Å. Given its cubic symmetry, all these bond distances can be represented as a multiple of the lattice constant and, in principle, only varying the lattice constant should give a good fit. However, this model does not fit the experimental data satisfactorily (see Fig. S5(b) in the Supplemental Material [29]), whereas a better fit is achieved by independently varying the individual bond distances, as shown in Fig. 11, and the obtained fitting parameters are listed in Table III. The

TABLE III. The coordination number (CN), bond distance (R), and thermal mean square variation (σ^2) from the EXAFS data fitting for $x = 0.25$. R_{eff} represents the expected bond distance calculated from the experimental lattice constant.

Bond type	CN	R_{eff}	R(Å)	σ^2(Å^2)
		Ti K-edge		
Ti-Fe	8	2.623	2.613(5)	0.00376(38)
Ti-Sn	6	3.029	3.023(9)	0.00543(76)
		Fe K-edge		
Fe-Sn	4	2.623	2.621(1)	0.00307(15)
Fe-Ti/Mn	4	2.623	2.596(3)	0.00568(45)
Fe-Fe	6	3.029	3.008(4)	0.00767(43)

notable aspect is the Fe–Ti bond distance discrepancy when viewed separately from the Fe and Ti edges. From the Ti edge, the Ti–Fe bond distance comes out to be ∼2.613 Å, consistent with the value derived from the lattice constant, whereas the same bond distance, when viewed from the Fe edge, yields a value of 2.596 Å. Furthermore, the Fe–Sn bond distance observed from the Fe edge is 2.621 Å, which aligns well with the lattice constant. This observation contradicts the expectations of the cubic symmetry, where Fe–Ti and Fe–Sn bond distances should be equidistant from the Fe atom. This discrepancy in the Fe–Ti correlation comes from the fact that Mn replaces some Ti atoms in $Fe_2Ti_{1-x}Mn_xSn$ compositions, and the bond distance involving the Ti site represents an average distance of Fe–Ti and Fe–Mn. This further indicates that in the Fe–(Ti/Mn) correlation, where Mn occupies the vacant Ti sites, the local lattice environment is distorted, leading to variations in the bond distance. These observations confirm that the lowering of local symmetry causes the random anisotropy in $Fe_2Ti_{1-x}Mn_xSn$ compositions.

Thus, the analysis of *ab initio* DOS calculation, resistivity, and magnetic data suggests that Mn substitution in Fe_2TiSn introduces localized moments. These local moments exhibit strong coupling with the conduction electron, which screens the interaction between two Mn atoms. As a result of this screening, the strength of the magnetic interaction decreases with increasing Mn-Mn distance, and typical ferromagnetic order is absent in $Fe_2Ti_{1-x}Mn_xSn$. To verify this, we have calculated the distance-dependent magnetic exchange interaction ($J_{\text{Mn-Mn}}$) between two Mn atoms. Estimating distance-dependent Mn-Mn magnetic interaction with smaller unit cells (considered for 25% substitution) is difficult. This is because, at large Mn-Mn separation in a small unit cell, contributions from the periodic images of Mn atoms at relatively shorter distances will start contributing to the magnetic energy. To avoid this problem, one has to consider a large supercell. We consider a 2×2×2 supercell and replace two Ti atoms with Mn atoms. The distance-dependent Mn-Mn magnetic interaction ($J_{\text{Mn-Mn}} = E_{\text{AFM}}$-$E_{\text{FM}}$) is then estimated as explained in the Experimental and Computational Details section. Here, we take advantage of the fact that the magnetic moments on Fe and Ti atoms are negligibly small, and hence, their insignificant direct contributions to $J_{\text{Mn-Mn}}$ can safely be ignored. The plot of separation dependent $J_{\text{Mn-Mn}}$ is shown in Fig. 12. One can observe that the effective Mn-Mn interaction is ferromagnetic, consistent with the experimental findings. This ferromagnetic interaction exponentially decreases with the Mn-Mn separation and becomes negligible at the separation of 8.51 Å.

It is important to emphasize that low-temperature resistivity and isothermal magnetization measurements reveal the coexistence of two seemingly contrasting phenomena: the Kondo effect and ferromagnetic order. Although these behaviors may appear mutually exclusive, several prior studies have reported their coexistence in correlated electron systems, particularly in certain heavy-fermion materials [4,5,52–54]. To further probe this interplay in our system, we have measured the specific heat of $x = 0.25$ at $H = 0$ T, as shown in Fig. 13(a). Above the magnetic transition temperature, the specific heat data can be described by the standard formula $C(T) = \gamma T + \beta T^3$, where the first and second terms represent the

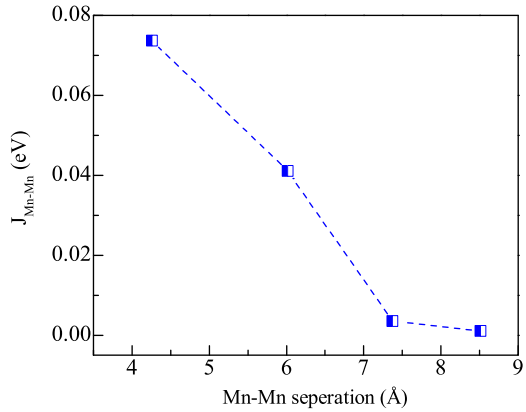


FIG. 12. Mn-Mn magnetic interaction at various separations in the unit cell of $x = 0.25$. For details, refer to the Experimental and Computational Details section.

electronic and lattice contributions to the $C(T)$. The linear fit of the C/T vs T^2 plot, as shown by the straight lines in Fig. 13(b), yields a moderately enhanced value of the Sommerfeld constant, $\gamma = 54.87 \pm 0.45$ mJ/mol-K^2. Notably, γ for $x = 0.25$ is more than twice the value reported for pristine Fe_2TiSn [16]. The γ values ranging from a few mJ/mol-K^2 to 2500 mJ/mol-K^2 are not uncommon in Kondo systems [55,56]. An estimate of the Debye temperature (θ_D) is obtained from the β using the relation $\beta = 12\pi^4 nR/5\theta_D$, where n and R represent the number of atoms in the formula unit and universal gas constant, respectively. The value of the θ_D obtained here is $\sim$359.3 $\pm$ 1.2 K. Specific heat measurements have been presented for the $x = 0.25$ composition, as it uniquely exhibits both Kondo-like electrical transport and magnetic ordering, making it the most representative sample for capturing the system's complex correlated behavior. Expanding this study to include a systematic, composition-dependent investigation of the Sommerfeld coefficient across the entire series would provide valuable insight into the evolution of effective mass and electronic correlations in this system. While such a detailed investigation lies beyond the scope of the present study, it represents a promising direction that can be pursued independently in future investigations of this correlated electron system.

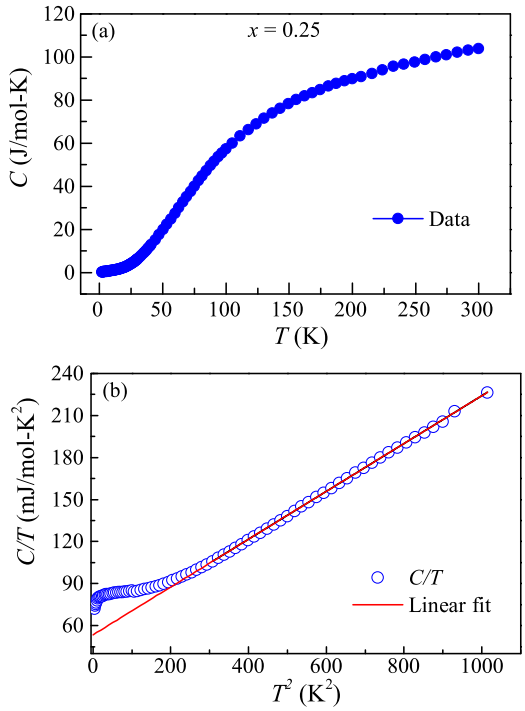


FIG. 13. (a) The temperature variation of specific heat of $x = 0.25$ at an applied field of 0 T, and (b) the specific-heat data in the form C/T versus T^2, along with the linear fit to the experimental data from high temperature to magnetic transition temperature (T_C).

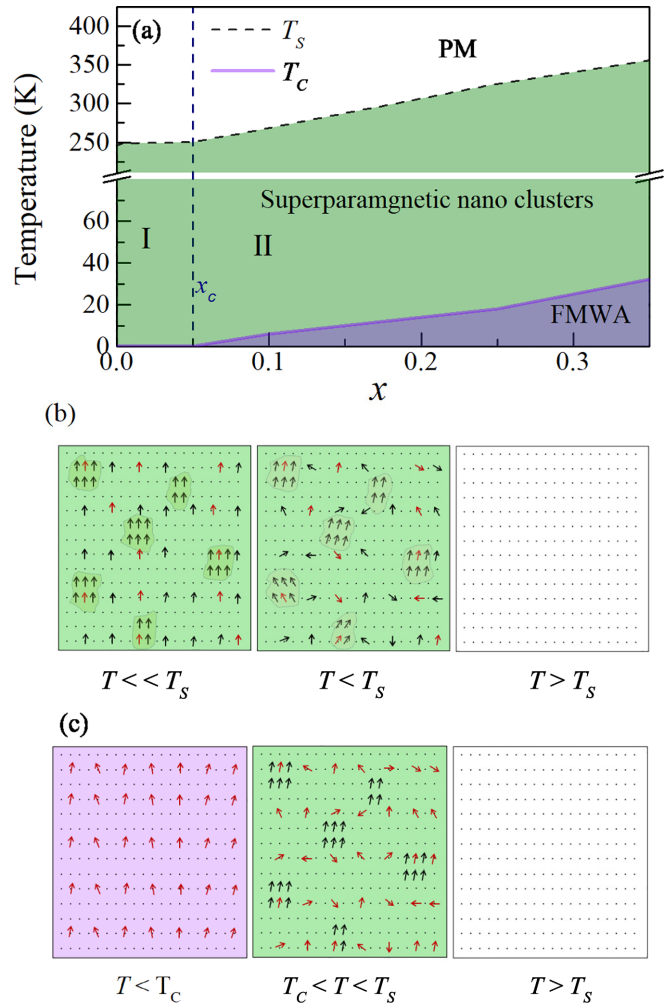


FIG. 14. (a) x-T phase diagram representing the change in the magnetic state of $Fe_2Ti_{1-x}Mn_xSn$ with temperature. (b) and (c) represents the schematic diagram of the magnetic state as a function of temperature in regions I and II, respectively. The local Mn moments (red arrow) align at an angle with the direction of the applied magnetic field.

Hence, according to the results of magnetic measurements, the magnetic state of $Fe_2Ti_{1-x}Mn_xSn$ changes with temperature as marked in the x-T phase diagram, as shown in Fig. 14(a). $Fe_2Ti_{1-x}Mn_xSn$ is in a typical PM state when the temperature is higher than T_s. As temperature decreases, ferromagnetic correlation appears due to the formation of magnetic clusters. In the case of $x < x_c$ (region I), clusters

continue to evolve with falling temperatures and lead to a superparamagnetic ground state, and no long-range magnetic order is observed in this region. The simplified schematic diagram of the magnetic state as a function of temperature is presented in Figs. 14(b) and 14(c). Substituting higher Mn content ($x > x_c$) in place of Ti in $Fe_2Ti_{1-x}Mn_xSn$ significantly alters this magnetic behavior. The strong local moments of Mn suppress the influence of high-temperature FM clusters on the low-temperature magnetic ground state and result in an unconventional ferromagnetic ordering driven by random anisotropy, known as the ferromagnet with wandering axis state, as represented as region II in the phase diagram. This transition from a superparamagnetic state in Fe_2TiSn to a weak random anisotropy-driven state with Mn substitution underscores the significant impact of Mn substitution on the magnetic properties of Heusler alloys. Furthermore, as confirmed from electrical resistivity and magnetic measurements and further supported through our DFT calculations, Mn substitution induces half-metallicity in the $Fe_2Ti_{1-x}Mn_xSn$, enhancing its potential for spintronic applications.

IV. CONCLUSION

This study investigated structural, magnetic, and transport properties of Mn-substituted Fe_2TiSn through room temperature XRD, temperature- and field-dependent magnetization, and magnetotransport measurements. Room temperature XRD patterns confirm the single-phase formation of all the compositions with ordered $L2_1$ structure. The temperature variation of electrical resistivity $Fe_2Ti_{1-x}Mn_xSn$ shows an overall increase in the magnitude with increasing Mn content. For $x \geqslant 0.25$, $\rho(T)$ shows a negative temperature coefficient of resistance, followed by an upturn at $T < 20$ K due to Kondo-like scattering and EEI. High-temperature electrical transport measurements, combined with the density of states calculation, indicate the possible formation of spin-polarized electronic structures and suggest half-metallicity in Mn-substituted Fe_2TiSn. Magnetization measurements display features indicative of weak anisotropy in the system, and low-temperature $M(H)$ behavior aligns with the random anisotropy model, suggesting that a ferromagnet with a wandering axis can be an apt description of the magnetic ground state of the $Fe_2Ti_{1-x}Mn_xSn$ compositions. The local lattice distortion in the prepared compositions leads to weak random anisotropy, affecting the overall magnetic properties.

ACKNOWLEDGMENTS

K.M. acknowledges DST-INSPIRE (File No. DST/INSPIRE/03/2021/001384/IF190777), New Delhi, for providing the research fellowship. K.M. and P.A.B. thank Doctor M. Gupta, UGC-DAE CSR, Indore, for extending the x-ray diffraction facility. S.K.P. thanks NFSG grant from BITS-Pilani, Dubai campus, which supported this research. Acknowledgment also goes to Professor J. G. Lin, Center for Condensed Matter Science, National Taiwan University, Taipei, Taiwan, for providing access to the magnetic measurement facility. We also thank Professor P. Raychaudhuri and G. Jangam for their help in magnetic measurement at the Tata Institute of Fundamental Research, Mumbai. K.M. thanks R. Joshi, UGC-DAE CSR, for helping with electrical transport measurements. Part of this research was carried out at the light source PETRA III at DESY, a member of the Helmholtz Association (HGF). K.M. and P.A.B. thank Edmund Welter for his assistance in using the photon beamline P65. We acknowledge financial support from the Department of Science and Technology (Govt. of India) provided within the framework of the India@DESY collaboration.

DATA AVAILABILITY

The data that support the findings of this article are not publicly available. The data are available from the corresponding author upon reasonable request.

[1] M. A. Ruderman and C. Kittel, Indirect exchange coupling of nuclear magnetic moments by conduction electrons, Phys. Rev. **96**, 99 (1954).

[2] K. Yosida, Magnetic properties of Cu-Mn alloys, Phys. Rev. **106**, 893 (1957).

[3] T. Kasuya, A theory of metallic ferro-and antiferromagnetism on Zener's model, Prog. Theor. Phys. **16**, 45 (1956).

[4] O. O. Bernal, D. D. MacLaughlin, H. G. Lukefahr, and B. Andraka, Copper NMR and thermodynamics of $UCu_{5-x}Pd_x$: Evidence for Kondo disorder, Phys. Rev. Lett. **75**, 2023 (1995).

[5] N. T. Huy, A. Gasparini, J. C. P. Klaasse, A. de Visser, S. Sakarya, and N. H. van Dijk, Ferromagnetic quantum critical point in URhGe doped with Ru, Phys. Rev. B **75**, 212405 (2007).

[6] A. Fernandez-Pañella, D. Braithwaite, B. Salce, G. Lapertot, and J. Flouquet, Ferromagnetism in $YbCu_2Si_2$ at high pressure, Phys. Rev. B **84**, 134416 (2011).

[7] J. Chen, Z. Dong, Q. Li, B. Ge, J. Zhang, Y. Zhang, and J. Luo, Enhanced thermoelectric performance in vacancy-filling Heuslers due to Kondo-like effect, Adv. Mater. **36**, 2405858 (2024).

[8] T. Krenke, E. Duman, M. Acet, E. F. Wassermann, X. Moya, L. Mañosa, and A. Planes, Inverse magnetocaloric effect in ferromagnetic Ni–Mn–Sn alloys, Nat. Mater. **4**, 450 (2005).

[9] P. A. Bhobe, K. R. Priolkar, and A. K. Nigam, Room temperature magnetocaloric effect in Ni–Mn–In, Appl. Phys. Lett. **91**, 242503 (2007).

[10] S. J. Hashemifar, P. Kratzer, and M. Scheffler, Preserving the half-metallicity at the Heusler alloy $Co_2MnSi(001)$ surface: A density functional theory study, Phys. Rev. Lett. **94**, 096402 (2005).

[11] M. Jourdan, J. MinÃ¡r, J. Braun, A. Kronenberg, S. Chadov, B. Balke, A. Gloskovskii, M. Kolbe, H. Elmers, G. Schönhense, H. Ebert, C. Felser, and M. Kläui, Direct observation of half-metallicity in the Heusler compound Co_2MnSi, Nat. Commun. **5**, 3974 (2014).

[12] C. L. Seaman, N. R. Dilley, M. C. de Andrade, J. Herrmann, M. B. Maple, and Z. Fisk, Superconductivity and magnetism

in the Heusler alloys MPd$_2$Pb (M=rare earth, Th, and U), Phys. Rev. B **53**, 2651 (1996).

[13] F. Garmroudi, I. Serhiienko, M. Parzer, S. Ghosh, P. Ziolkowski, G. Oppitz, H. D. Nguyen, C. Bourgès, Y. Hattori, A. Riss *et al.*, Decoupled charge and heat transport in Fe$_2$VAl composite thermoelectrics with topological-insulating grain boundary networks, Nat. Commun. **16**, 2976 (2025).

[14] M. Parzer, F. Garmroudi, A. Riss, M. Reticcioli, R. Podloucky, M. Stöger-Pollach, E. Constable, A. Pustogow, T. Mori, and E. Bauer, Semiconducting Heusler compounds beyond the Slater-Pauling rule, PRX Energy **3**, 033006 (2024).

[15] I. Galanakis, P. H. Dederichs, and N. Papanikolaou, Slater-Pauling behavior and origin of the half-metallicity of the full-Heusler alloys, Phys. Rev. B **66**, 174429 (2002).

[16] S. Chaudhuri, P. A. Bhobe, A. Bhattacharya, and A. K. Nigam, Unraveling the physical properties and superparamagnetism in anti-site disorder controlled Fe$_2$TiSn, J. Phys.: Condens. Matter **31**, 045801 (2019).

[17] A. Ślebarski, M. B. Maple, E. J. Freeman, C. Sirvent, D. Tworuszka, M. Orzechowska, A. Wrona, A. Jezierski, S. Chiuzbaian, and M. Neumann, Weak ferromagnetism induced by atomic disorder in Fe$_2$TiSn, Phys. Rev. B **62**, 3296 (2000).

[18] A. Ślebarski, M. B. Maple, A. Wrona, and A. Winiarska, Kondo-type behavior in Fe$_{2-x}M_x$TiSn (M = Co, Ni), Phys. Rev. B **63**, 214416 (2001).

[19] M. Häfner, J. K. Viljas, D. Frustaglia, F. Pauly, M. Dreher, P. Nielaba, and J. C. Cuevas, Theoretical study of the conductance of ferromagnetic atomic-sized contacts., Phys. Rev. B **77**, 104409 (2008).

[20] S. Chaudhuri, P. A. Bhobe, and A. K. Nigam, Possible half-metallicity and variable range hopping transport in Sb-substituted Fe$_2$TiSn Heusler alloys, J. Phys.: Condens. Matter **30**, 015703 (2018).

[21] S. Chaudhuri, D. Salas, V. Srihari, E. Welter, I. Karaman, and P. A. Bhobe, Half metallicity in Cr substituted Fe$_2$TiSn, Sci. Rep. **11**, 524 (2021).

[22] B. Ravel and M. Newville, *ATHENA, ARTEMIS, HEPHAESTUS*: Data analysis for X-ray absorption spectroscopy using *IFEFFIT*, J. Synchrotron Radiat. **12**, 537 (2005).

[23] P. Giannozzi, O. Andreussi, T. Brumme, O. Bunau, M. B. Nardelli, M. Calandra, R. Car, C. Cavazzoni, D. Ceresoli, M. Cococcioni, N. Colonna, I. Carnimeo, A. D. Corso, S. de Gironcoli, P. Delugas, R. A. DiStasio, A. Ferretti, A. Floris, G. Fratesi, G. Fugallo *et al.*, Advanced capabilities for materials modeling with QUANTUM ESPRESSO, J. Phys.: Condens. Matter **29**, 465901 (2017).

[24] P. Giannozzi, S. Baroni, N. Bonini, M. Calandra, R. Car, C. Cavazzoni, D. Ceresoli, G. L. Chiarotti, M. Cococcioni, I. Dabo *et al.*, QUANTUM ESPRESSO: A modular and open-source software project for quantum simulations of materials, J. Phys.: Condens. Matter **21**, 395502 (2009).

[25] D. Vanderbilt, Soft self-consistent pseudopotentials in a generalized eigenvalue formalism, Phys. Rev. B **41**, 7892 (1990).

[26] J. P. Perdew, K. Burke, and M. Ernzerhof, Generalized gradient approximation made simple, Phys. Rev. Lett. **77**, 3865 (1996).

[27] J. Rodríguez-Carvajal, Recent advances in magnetic structure determination by neutron powder diffraction, Phys. B: Condens. Matter **192**, 55 (1993).

[28] A. R. Denton and N. W. Ashcroft, Vegard's law, Phys. Rev. A **43**, 3161 (1991).

[29] See Supplemental Material at http://link.aps.org/supplemental/10.1103/jnxr-9qf8 for Rietveld refinement of XRD data, lattice parameters for all compositions, normalized electrical resistivity of all the compositions, and the k^2-weighted EXAFS extracted from raw absorption spectra. The fittings to low-temperature resistivity, isothermal magnetization, and EXAFS spectra for $x = 0.25$ composition are also included here.

[30] P. A. Lee and T. V. Ramakrishnan, Disordered electronic systems, Rev. Mod. Phys. **57**, 287 (1985).

[31] S. Chaudhuri, V. Srihari, A. K. Nigam, and P. A. Bhobe, Origin of the magnetic ground state developed upon Si, Ge, and Sb-substitution at Sn site in Fe$_2$TiSn, J. Appl. Phys. **126**, 083904 (2019).

[32] S. Chatterjee, S. Chatterjee, S. Giri, and S. Majumdar, Transport properties of Heusler compounds and alloys, J. Phys.: Condens. Matter **34**, 013001 (2022).

[33] A. Chanda, D. Rani, J. Nag, A. Alam, K. G. Suresh, M. H. Phan, and H. Srikanth, Emergence of asymmetric skew-scattering dominated anomalous Nernst effect in the spin gapless semiconductors Co$_{1+x}$Fe$_{1-x}$CrGa, Phys. Rev. B **106**, 134416 (2022).

[34] S. Ouardi, G. H. Fecher, C. Felser, and J. Kubler, Realization of spin gapless semiconductors: The Heusler compound Mn$_2$CoAl, Phys. Rev. Lett. **110**, 100401 (2013).

[35] D. Gnida, K. Ciesielski, and D. Kaczorowski, Origin of the negative temperature coefficient of resistivity in the half-Heusler antimonides LuNiSb and YPdSb, Phys. Rev. B **103**, 174206 (2021).

[36] Y. Venkateswara, S. Gupta, S. S. Samatham, M. R. Varma, Enamullah, K. G. Suresh, and A. Alam, Competing magnetic and spin-gapless semiconducting behavior in fully compensated ferrimagnetic CrVTiAl: Theory and experiment, Phys. Rev. B **97**, 054407 (2018).

[37] L. Bainsla, A. I. Mallick, M. M. Raja, A. A. Coelho, A. K. Nigam, D. D. Johnson, A. Alam, and K. G. Suresh, Origin of spin gapless semiconductor behavior in CoFeCrGa: Theory and experiment, Phys. Rev. B **92**, 045201 (2015).

[38] A. Ślebarski, Electron-correlation effects in a disordered Fe$_2$TiSn Heusler alloy, J. Phys. D: Appl. Phys. **39**, 856 (2006).

[39] P. A. Lee and T. V. Ramakrishnan, Magnetoresistance of weakly disordered electrons, Phys. Rev. B **26**, 4009 (1982).

[40] V. Hien-Hoang, N. Chung, and H. Kim, Electrical transport properties and Kondo effect in La$_{1-x}$Pr$_x$NiO$_{3-\delta}$ thin films, Sci. Rep. **11**, 5391 (2021).

[41] S. Ghosh, R. G. Tanguturi, P. Pramanik, D. C. Joshi, P. K. Mishra, S. Das, and S. Thota, Low-temperature anomalous spin correlations and Kondo effect in ferromagnetic SrRuO$_3$/LaNiO$_3$/La$_{0.7}$Sr$_{0.3}$MnO$_3$ trilayers, Phys. Rev. B **99**, 115135 (2019).

[42] R. Dey, T. Pramanik, A. Roy, A. Rai, S. Guchhait, S. Sonde, H. C. P. Movva, L. Colombo, L. F. Register, and S. K. Banerjee, Strong spin-orbit coupling and Zeeman spin splitting in angle-dependent magnetoresistance of Bi$_2$Te$_3$, Appl. Phys. Lett. **104**, 223111 (2014).

[43] T. Sekitani, M. Naito, and N. Miura, Kondo effect in underdoped n-type superconductors., Phys. Rev. B **67**, 174503 (2003).

[44] R. Jha, N. Tsujii, F. Garmroudi, S. Khmelevskyi, E. Bauer, and T. Mori, Unexpected p-type thermoelectric transport

arising from magnetic Mn substitution in $Fe_2V_{1-x}Mn_xAl$ Heusler compounds, J. Mater. Chem. C **12**, 8861 (2024).

[45] S. Sato, S. Irie, Y. Nagamine, T. Miyazaki, and Y. Umeda, Antiferromagnetism in perfectly ordered $L1_0$-MnAl with stoichiometric composition and its mechanism, Sci. Rep. **10**, 12489 (2020).

[46] E. M. Chudnovsky, W. M. Saslow, and R. A. Serota, Ordering in ferromagnets with random anisotropy, Phys. Rev. B **33**, 251 (1986).

[47] R. Saha, V. Srinivas, and T. V. Chandrasekhar Rao, Evolution of ferromagnetic-like order in $Fe_2V_{1-x}Cr_xAl$, Phys. Rev. B **79**, 174423 (2009).

[48] M. Vasundhara, V. Srinivas, and V. V. Rao, Evidence for cluster glass behavior in Fe_2VAl Heusler alloys, Phys. Rev. B **78**, 064401 (2008).

[49] S. Mondal, C. Mazumdar, R. Ranganathan, E. Alleno, P. C. Sreeparvathy, V. Kanchana, and G. Vaitheeswaran, Ferromagnetically correlated clusters in semimetallic Ru_2NbAl Heusler alloy and its thermoelectric properties., Phys. Rev. B **98**, 205130 (2018).

[50] P. M. Gehring, M. B. Salamon, A. del Moral, and J. I. Arnaudas, Magnetic static and scaling properties of the weak random-axis magnet $Dy_xY_{1-x}Al_2$, Phys. Rev. B **41**, 9134 (1990).

[51] R. Fisch, Cubic models with random anisotropy, Phys. Rev. B **48**, 15764 (1993).

[52] J. Zhang, Y. Xu, S. Cao, G. Cao, Y. Zhang, and C. Jing, Kondo-like transport and its correlation with the spin-glass phase in perovskite manganites, Phys. Rev. B **72**, 054410 (2005).

[53] H. Yang, S.-H. Yang, G. Ilnicki, J. Martinek, and S. S. P. Parkin, Coexistence of the Kondo effect and a ferromagnetic phase in magnetic tunnel junctions, Phys. Rev. B **83**, 174437 (2011).

[54] S. Barua, M. C. Hatnean, M. R. Lees, and G. Balakrishnan, Signatures of the Kondo effect in VSe_2, Sci. Rep. **7**, 10964 (2017).

[55] A. D. Hillier, D. T. Adroja, S. R. Giblin, W. Kockelmann, B. D. Rainford, and S. K. Malik, Understanding the heavy fermion behavior in $CeInPt_4$, Phys. Rev. B **76**, 174439 (2007).

[56] M. Jaime, R. Movshovich, G. R. Stewart, W. P. Beyermann, M. G. Berisso, M. F. Hundley, P. C. Canfield, and J. L. Sarrao, Closing the spin gap in the Kondo insulator $Ce_3Bi_4Pt_3$ at high magnetic fields, Nature (London) **405**, 160 (2000).